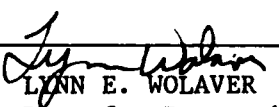


MICROCOPY RESOLUTION TEST CHART
NATIONAL BUREAU OF STANDARDS-1963-A

①

SECURITY CLASSIFICATION OF THIS PAGE (When Data Entered)

REPORT DOCUMENTATION PAGE		READ INSTRUCTIONS BEFORE COMPLETING FORM	
1. REPORT NUMBER AFIT/CI/NR 86- 111T	2. GOVT ACCESSION NO.	3. RECIPIENT'S CATALOG NUMBER	
4. TITLE (and Subtitle) Laser Beam Degradation by an Inhomogeneous Free Jet Mixing Layer		5. TYPE OF REPORT & PERIOD COVERED THESIS/DISSERTATION/	
		6. PERFORMING ORG. REPORT NUMBER	
7. AUTHOR(s) David Barnett Higgins		8. CONTRACT OR GRANT NUMBER(s)	
9. PERFORMING ORGANIZATION NAME AND ADDRESS AFIT STUDENT AT: University of Washington		10. PROGRAM ELEMENT, PROJECT, TASK AREA & WORK UNIT NUMBERS	
11. CONTROLLING OFFICE NAME AND ADDRESS AFIT/NR WPAFB OH 45433-6583		12. REPORT DATE 1986	
		13. NUMBER OF PAGES 65	
14. MONITORING AGENCY NAME & ADDRESS (if different from Controlling Office)		15. SECURITY CLASS. (of this report) UNCLAS	
		15a. DECLASSIFICATION/DOWNGRADING SCHEDULE	
16. DISTRIBUTION STATEMENT (of this Report) APPROVED FOR PUBLIC RELEASE; DISTRIBUTION UNLIMITED			
17. DISTRIBUTION STATEMENT (of the abstract entered in Block 20, if different from Report) B			
18. SUPPLEMENTARY NOTES APPROVED FOR PUBLIC RELEASE: IAW AFR 190-1		 LYNN E. WOLAVER 8 Aug 86 Dean for Research and Professional Development AFIT/NR	
19. KEY WORDS (Continue on reverse side if necessary and identify by block number)			
20. ABSTRACT (Continue on reverse side if necessary and identify by block number) ATTACHED. DTIC FILE COPY			

University of Washington

Abstract

LASER BEAM DEGRADATION
BY AN INHOMOGENEOUS FREE JET MIXING LAYER

by David B. Higgins

Chairperson of the Supervisory Committee:
Professor Walter H. Christiansen
Department of Aeronautics and Astronautics

A method for directly sampling and numerically processing the far field diffraction pattern of laser beams was developed. This method was used to examine the distortion effects of subsonic mixing layers with zero velocity ratio and various density ratios on beams passing through them. Details of the method are presented. Strehl ratios, indicating the amount of beam degradation, are derived from the data obtained from beams having passed through the mixing layers. The Strehl ratios derived from the data were found to match reasonably well with theoretical predictions.

X



Accession For	
NTIS GRA&I	<input checked="" type="checkbox"/>
DTIC TAB	<input type="checkbox"/>
Unannounced	<input type="checkbox"/>
Justification	
By _____	
Distribution _____	
Availability _____	
Dist	
A-1	

111

Laser Beam Degradation
By an Inhomogeneous Free Jet Mixing Layer
by
DAVID BARNETT HIGGINS

A thesis submitted in partial fulfillment
of the requirements for the degree of

Master of Engineering

University of Washington

1986

Approved by Walter H. Christensen
(Chairperson of Supervisory Committee)

Program Authorized
to Offer Degree Aeronautics and Astronautics

Date 5/16/86

In presenting this thesis in partial fulfilment of the requirements for a Master's degree at the University of Washington, I agree that the Library shall make its copies freely available for inspection. I further agree that extensive copying of this thesis is allowable only for scholarly purposes, consistent with "fair use" as prescribed in the U. S. Copyright Law. Any other reproduction for any purposes or by any means shall not be allowed without my written permission.

Signature Daniel B. Higgins

Date 13 May 1986

TABLE OF CONTENTS

	Page
List of Figures	iii
List of Tables	iv
Chapter I: INTRODUCTION	1
Chapter II: THE MIXING LAYER	4
Chapter III: EXPERIMENTAL APPARATUS	14
Gas Jet and Test Section	14
Optical Bench	16
Data Acquisition Equipment	20
Chapter IV: CALIBRATION AND CHECK OF EXPERIMENTAL SYSTEM	21
Chapter V: PROCEDURES	30
Chapter VI: DATA	34
Chapter VII: DATA REDUCTION	45
Chapter VIII: DISCUSSION	55
Chapter IX: CONCLUSIONS	60
REFERENCE LIST	63

LIST OF FIGURES

Number	Page
1. Mixing Layer	6
2. Deflection of a light ray	9
3. Equipment arrangement	15
4. Nozzle and test section	17
5. Airy pattern	23
6. Intensity integration	25
7. Normalizing effect on intensity integration	26
8. The effect of jet generated noise	29
9. Pixel response plot	35
10. Pseudo-3-D intensity plot for 62%He/38%Ar	38
11. Pseudo-3-D intensity plot for CO ₂	39
12. Beam distortion resulting from a CO ₂ jet	40
13. Pseudo-3-D intensity plot for He	42
14. Pseudo-3-D intensity plot for 62%He/38%Ar	43
15. Pseudo-3-D intensity plot for 38%He/62%Ar	43
16. Pseudo-3-D intensity plot for N ₂	44
17. Pseudo-3-D intensity plot for CO ₂	44
18. Power plots for an undegraded beam	50
19. Power plots for a 62%He/38% He jet	52
20. Measured Strehl ratios	56
21. Measured beam deflections	59

LIST OF TABLES

Number	Page
1. Test conditions	36
2. Average Strehl ratios 1 cm downstream	53
3. Average Strehl ratios 2 cm downstream	54

ACKNOWLEDGMENTS

The author wishes to express his gratitude to Professor Christiansen for his guidance and compassion in his direction of this project. He understood well the problems of an Air Force officer returning to school after many years and on a short schedule. In addition, sincere thanks to Dr Dave Bogdanoff for his advice and many helpful suggestions on the execution of the experimental work. Special thanks go to Mac Saynor and Denny Peterson for their outstanding work and instruction in the machine shop. Special thanks also go to Andrew Westphal and Tom Blum for development of much of the software, assistance in the lab, and moral support. But, especially to my wife and daughter, without whose love, understanding, and encouragement, I never would have finished: thank you.

I. INTRODUCTION

Velocity sheared mixing layers, or shear layers, are an important design consideration for many high power lasers. Mixing layers will occur across openings in the skin of aircraft, for example, where some lasers may have application. And, they are found inside the laser itself in many instances: they can be generated in the laser resonator, and they are significant in aerodynamic windows¹.

In addition, the mixing layer is interesting in itself as the subject for research in fluid dynamics. Many recent research papers have examined the effects on light as it passes through a mixing layer. In some cases, a laser beam is used as a diagnostic tool to determine mixing layer characteristics based on the distortion in the near field of the beam after passing through the layer. In other cases it is the distortion itself which is the subject of research. Poling² (1985), for example, used near field interferometry (among other techniques) to study mixing layer spreading rates and density gradients. Christiansen et al³ (1984) did similar work, but also determined the mean square phase error for use in calculating the Strehl ratio⁴, I/I_0 , which is a useful quantity for measuring the degradation of the laser beam.

Legner et al⁵ (1978) and Vu et al⁶ (1980) developed models for the reduction in beam intensity at the peak of the far field distribution and obtained experimental data for the velocity matched mixing layer similar to that found in the aerodynamic window of a CO₂ laser. Wasserstrom et al⁷ demonstrated theoretically that a system of crossed jets (and their attendant shear layers) could be used to partially compensate for phase error caused by thermal blooming. In each of these, interferograms of the near field are the primary source of data on the distortion of the beam. From near field data one may compute the degradation that would be seen in the far field.

Georgouras⁸ (1980), on the other hand, measured the the far field degradation directly. By inserting various size circular apertures into the beam after it had passed through the mixing layer, he was able to measure the the average cross sectional distribution of beam power and compare it to the undistorted case.

This thesis describes a different technique that was used to obtain data directly from the far field of a laser beam after passing through a mixing layer. Further, it presents data obtained by the technique on a variety of mixing layers at two downstream locations and using two beam diameters. The work presented here is very similar to that of Georgouras in that the far field intensity

distribution is measured directly for circular beams passing through mixing layers generated by jets of various gases. The primary difference being the technique for measuring the far field intensity distribution of the beam. Gergeours used a mask to sample various portions of the degraded beam and a lens to focus the sampled portion onto a single photodiode to measure the power in that portion. Here, the majority of the beam's far field is captured simultaneously by a charge coupled device (CCD) camera array of 256 x 256 photodiodes. Other than the demagnification of the beam to shorten the distance to the far field, similar to Gergeours's, no lens is used to focus the light being sampled. This technique does not suffer from the requirement for a separate run for each region of the beam to be examined since it samples almost the entire beam at once. Nor does it depend on the mask being centered with respect to the distorted beam since it does not use this type of mask.

This thesis covers, in detail, the procedures used to obtain far field diffraction pattern images and their subsequent analysis. Even though the conditions addressed here were limited to zero velocity ratio layers with a range of density ratios from 0.195 to 7.22 at a Mach number of 0.1, it is the first step in developing this technique to cover the wider range of conditions of interest.

II. THE MIXING LAYER

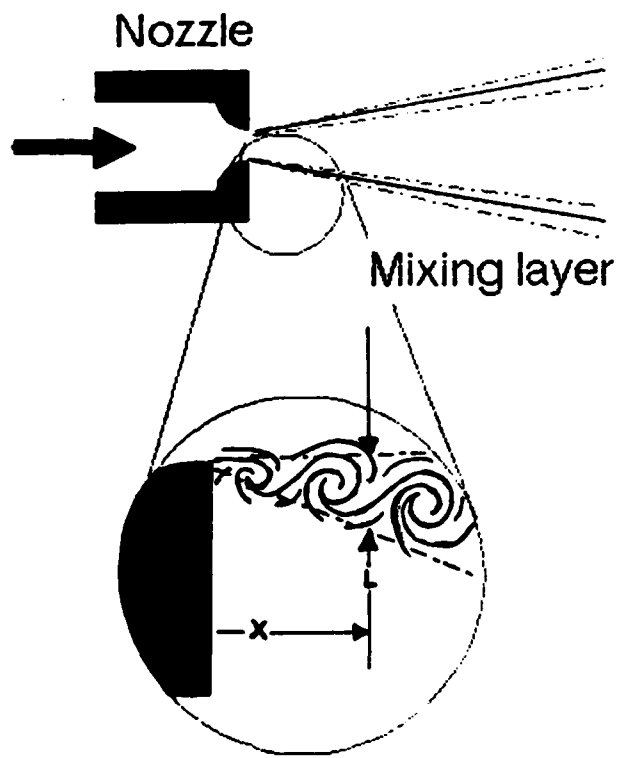
One type of turbulent mixing layer results from the flow of two adjacent fluid streams having different bulk velocities. The region of interface is called a velocity sheared mixing layer, or shear layer. The two streams may or may not be composed of the same fluid. Another type of mixing layer, composed of two streams having the same velocity but differing in some other property, is called a velocity matched mixing layer. While this latter type of mixing layer may be either turbulent or laminar, the former is almost always turbulent. Whether it is or not depends on the Reynolds number, but the critical Reynolds number, that Reynolds number below which disturbances in the flow are not amplified, for a jet⁹ is on the order of 10. Only the turbulent, velocity sheared mixing layer is discussed here.

Specifically, the zero velocity ratio mixing layer occurring at the boundaries of a free gas jet were examined for their degradation effects on normally incident laser beams. The velocity ratio for this mixing layer is zero because the smaller of the two fluid velocities is zero. (A velocity matched mixing layer would have a velocity ratio of one.) As the gas jet enters the stationary

surrounding gas, the boundary between the two gases is unstable because of the velocity discontinuity and resulting shear stress at the boundary. Very quickly, the boundary "rolls up" into vortices which mix the various properties of the two gases. As the vortices progress downstream they pair and combine with other vortices and grow in size, thus the region of mixing grows in thickness¹⁰. This growing region of vortices moving downstream is the turbulent, velocity sheared mixing layer. A sketch of such a layer is shown in figure 1.

The distance between the vortices as they are formed, and thus an indication of how far downstream from the nozzle they form, is expected to be proportional to boundary layer thickness at the nozzle exit¹¹, and by 1000 momentum thicknesses downstream the flow is self similar¹². Previous researchers² using the same nozzle that is used here have calculated the momentum thickness of the boundary layer. Using the Pohlhausen analysis with Walz's solution, as discussed in Schlichting¹³, for Mach number $M = 0.1$ the momentum thickness of the boundary layer at the nozzle exit has been calculated to be 0.0028 cm. Thus, the region of vortices should be well established 1 or 2 cm downstream.

Fig. 1. Mixing Layer. Sketch of a mixing layer
caused by a free jet.



One of the properties mixed by the vortices is the index of refraction. For a gas, the index of refraction may be obtained from¹⁴:

$$n = 1 + \beta \frac{\rho}{\rho_s} \quad (1)$$

Where

β = a tabulated constant

ρ = density

ρ_s = density at standard conditions

n = index of refraction,

and the tabulated constant, β , depends on the gas and the wavelength(s) of light being used.

Brown and Roshko¹⁰ demonstrated that, as predicted by theory¹³, the thickness of the mixing layer grows linearly with distance downstream, hence the mixing layer shape may be approximated as a wedge. According to Vu et. al.⁶ the thickness of this wedge, L , may be expressed as:

$$L = c \left(\frac{U_1 - U_2}{U_1 + U_2} \right) x \quad (2)$$

where:

x = distance downstream.

U_1 = x-velocity of high speed stream.

U_2 = x-velocity of low speed stream (zero in this case).

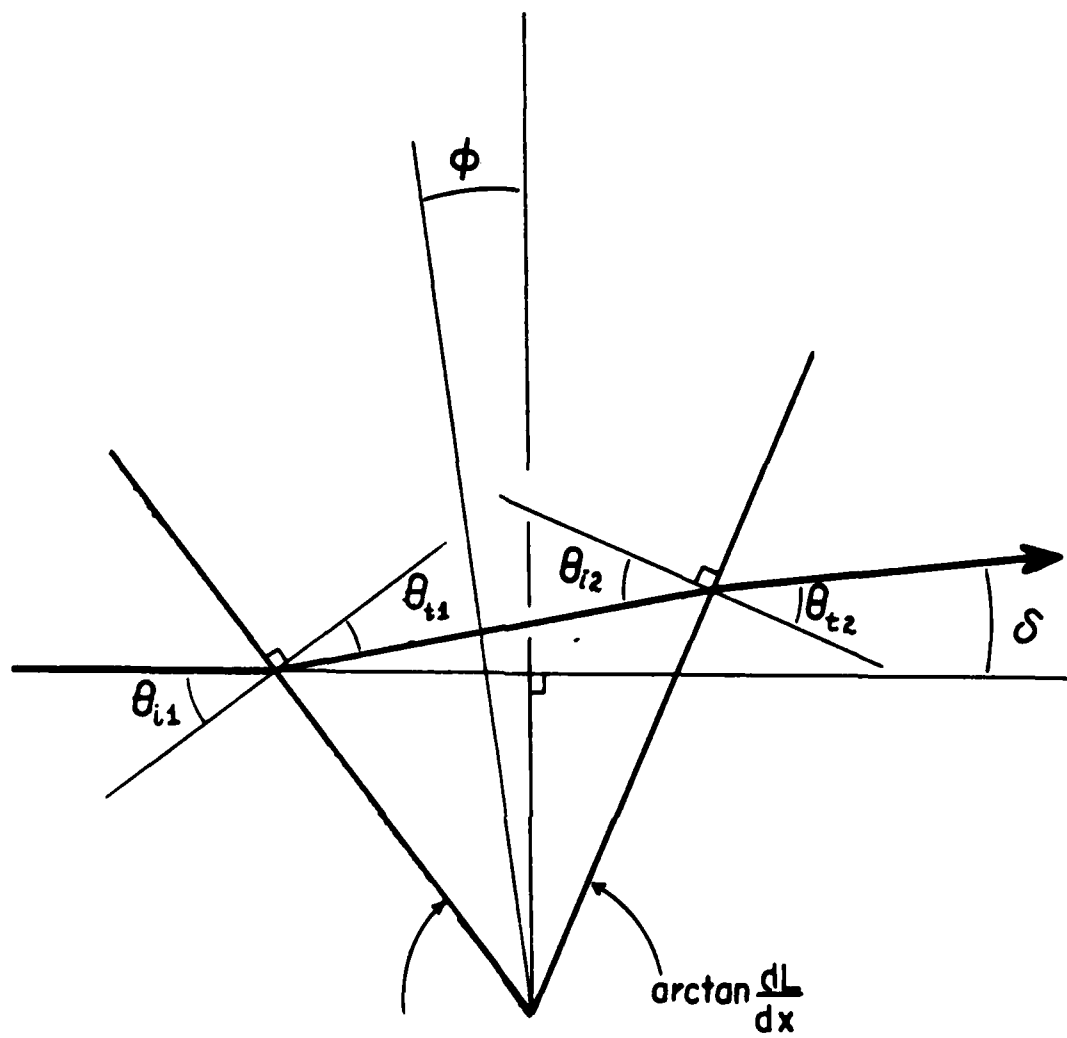
c = a constant for each mixing layer.

Brown and Roshko¹⁰ measured c and found it to be a weak function of density ratio having values of 0.51, 0.38, and 0.28 corresponding to density ratios of $\rho_2/\rho_1 = 7, 1,$ and $1/7$ respectively.

It is known however, that for the nozzle used here, the linear growth approximation given by eqn. (2) is only valid up to a distance of about 2 exit widths, or about 2.8 cm downstream². Nevertheless, if the layer is represented as a wedge shaped region having an index of refraction equal to the mean of the index of refraction of the two gases (air and the jet), then the beam would be deflected according to Snell's law at each of the two interfaces (see fig. 2):

$$n_1 \sin(\theta_1) = n_2 \sin(\theta_2) \quad (3)$$

Fig. 2. Deflection of a light ray passing through a wedge shaped region whose refractive index is the average of the refractive indices of the regions on either side of the wedge.



Thus, the total deflection of the beam is given by

$$\delta = \frac{1}{2} \arctan \left(\frac{dL}{dx} \right) - \theta_{t2} \quad (4)$$

Where:

$$\theta_{t2} = \arcsin \left\{ \frac{n_a + n_j}{2n_j} \sin(\gamma - \theta_{t1}) \right\}$$

$$\theta_{t1} = \arcsin \left\{ \frac{2n_a}{n_a + n_j} \sin \left(\frac{\gamma}{2} \right) \right\}$$

$$\theta_{i1} = \frac{\gamma}{2} + \phi$$

$$\theta_{i2} = \gamma - \theta_{t1}$$

and,

$\gamma = \arctan (dL/dx)$, the wedge angle.

n_a = refractive index of air.

n_j = refractive index of the jet.

δ = angular deflection of the ray.

ϕ = "tilt" of the wedge toward the incoming beam
(see fig. 2)

The values of δ predicted by eqn. (4) will be mentioned briefly in Discussion and Conclusion sections. Surprisingly enough though, eqn. (4) predicts that, for a homogeneous wedge, when ϕ is zero the angular deflection of the beam is essentially zero as well.

At best however, eqn. (4) is an estimate of the time averaged deflection of the beam. Because the vortices in the mixing layer are traveling through the beam as they move downstream they cause nonsteady effects as well. The vortices move at a speed which is the average between that of the jet and that of the air. Since the air is stationary, the vortices generated by a jet with $M = 0.1$, for example, move downstream at roughly 1700 cm/sec if the jet gas is nitrogen. For a helium jet their speed would be about 5000 cm/sec, and roughly 1300 cm/sec for a carbon dioxide jet.

In addition, the actual density distribution in the vortices is highly nonlinear. This means that the density

distribution across the mixing layer is nonlinear. This causes wavefront distortion to be added to the beam deflection or tilt. Vu et. al.⁶ have derived the following theoretical relationship to predict this degradation of the beam:

$$\frac{I_0 - I}{I} = \frac{1}{2} k^2 \Delta n^2 \alpha^2 c^2 \left(\frac{U_1 - U_2}{U_1 + U_2} \right)^2 x^2 \quad (5)$$

In this expression:

I_0 = nondegraded beam intensity at the center of the far field focus.

I = degraded beam intensity at the center of the far field focus.

k = wave number

Δn = index of refraction difference across the mixing layer.

α = a measured quantity.

The quantity α is proportional to the turbulence intensity and has a value close to that of the density or temperature fluctuations:

$$\frac{\sqrt{\rho'^2}}{\Delta\rho} \quad \text{and} \quad \frac{\sqrt{T'^2}}{\Delta T}$$

Batt¹⁵ has measured the temperature fluctuation to be approximately 0.15, while Fiedler¹⁶ measured it to be nearly 0.20.

In his 1969 paper, Sutton¹⁷ presented a relationship related to that in eqn. (5). In fact, the term on the right in eqn. (5) may be regarded as the first term in a Taylor series expansion of the right side of Sutton's 1969 relationship:

$$\frac{I_0 - I}{I_0} = 1 - \exp \left[-\frac{1}{2} k^2 \Delta n^2 \sigma^2 c^2 \left(\frac{U_1 - U_2}{U_1 + U_2} \right)^2 x^2 \right] \quad (6)$$

The left side of eqns. (5) and (6) is just one minus the Strehl ratio. The Strehl ratios obtained from eqn. (6) will be compared to measurements and discussed briefly in the Discussion and Conclusions sections.

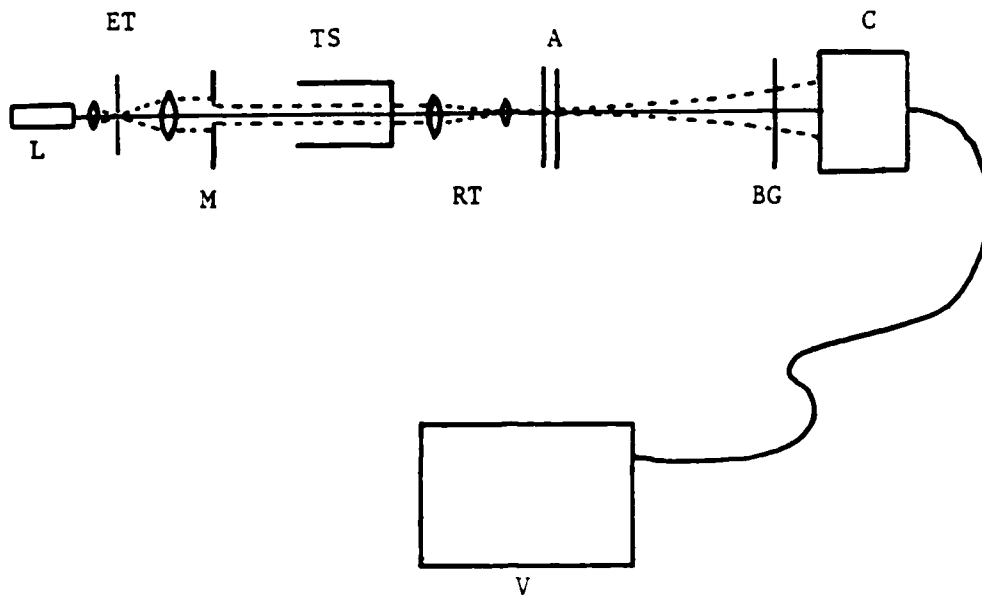
III. EXPERIMENTAL APPARATUS:

In order to measure the beam degradation for this experiment, the equipment arrangement sketched in figure 3 was used. The beam was spatially filtered, expanded, collimated, and then masked by a circular aperture to produce a parallel beam of nearly constant intensity distribution across a circular cross section. This beam was then passed through the mixing layer of a jet exiting a rectangular nozzle into a three sided rectangular test section with optical quality glass walls. The beam then entered a reducing telescope of sufficient power to bring the Fraunhofer far field diffraction pattern within convenient range of the optical bench. A charge coupled device (CCD) electronic camera then captured the image of the diffraction pattern for digital storage and analysis on a dedicated microcomputer. A detailed description of the equipment and experimental setup is given below.

Gas Jet and Test Section:

A custom built nozzle was used to produce the mixing layer. The nozzle was operated at a nominal Mach number of 0.1 with a variety of gases to generate mixing layers, in room air, having density ratios from .195 to 7.22. The

Fig. 3. Sketch of the equipment arrangement. ET is an expanding telescope with spatial filter. M is the aperture mask. TS is the test section. RT is the reducing telescope without spatial filter. A is the stack of attenuating neutral density filters. BG is the infrared filter. C is the CCD camera. V is the MicroVAX computer with Microtex camera driver and A/D board.



nozzle exit cross section was rectangular, 1.4 cm by 1.4 cm, and exited into a rectangular test section consisting of optical quality glass walls on three sides with the fourth side open to room air (see fig. 4). This configuration produced a free gas/air mixing layer at the open side of the test section. The laser beam entered the test section through the open side and mixing layer, and exited through the boundary layer and glass wall at the opposite side. The operation of the nozzle and quality of the mixing layer were verified by Schlieren photography. For a more detailed discussion of the nozzle, see Poling².

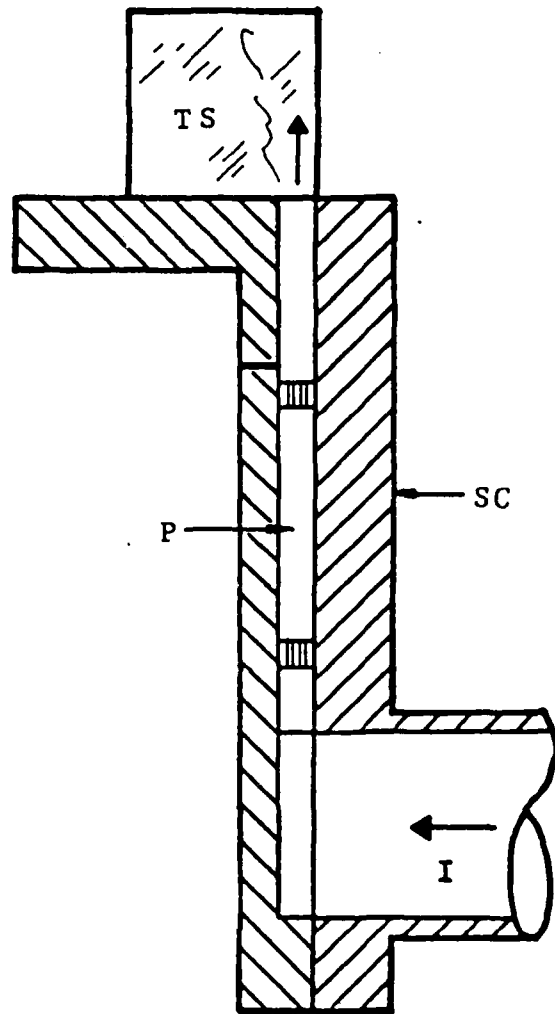
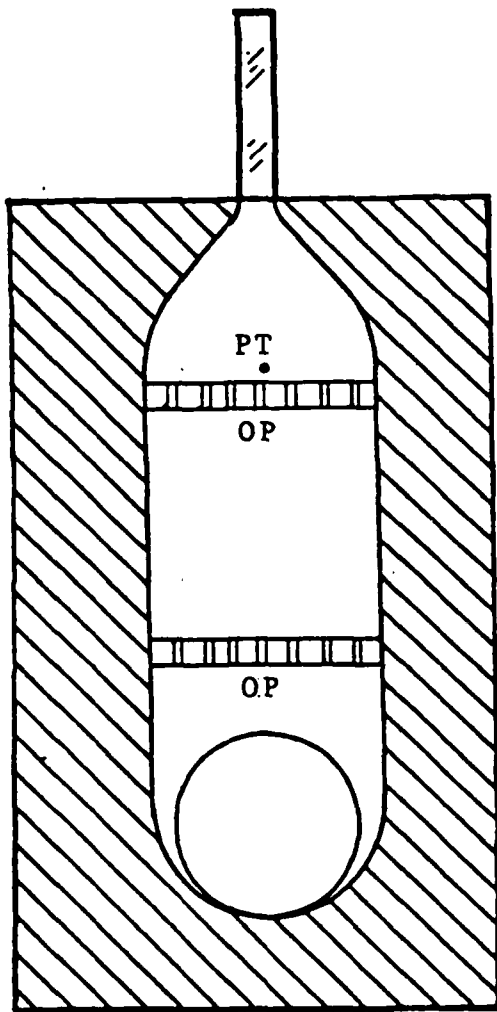
Optical Bench:

Laser: The laser used for this research was an unpolarized, continuous laser with a rated output of 0.95 milliwatt.

Beam Expander: The laser output beam was expanded from 1 mm to 5 cm in diameter and collimated by beam expander with a 25 micron spatial filter.

Mask: before entering the test section, the parallel beam from the expander was masked by a circular aperture machined in a 0.126 cm piece of aluminum.

Fig. 4. Nozzle and test section. I is the gas inlet. P is the plenum. SC is the side cover. OP are orifice plates. PT is a pressure tap. TS is the test section.



Reducing Telescope: The beam which exited the test section was demagnified by a 40 power beam expander without spatial filter oriented as a reducing telescope. The telescope was focused to produce the sharpest possible Airy¹⁸ pattern.

Camera: The far field pattern was placed directly on the CCD array of an EG&G Reticon camera model 9256-B. This camera has a 256x256 photodiode array. Depending upon the size of the mask in use and beam intensity at the photodiode array, the array was located between 30 cm and 75 cm from the output lens of the reducing telescope.

Optical Rail: A single extrusion of aluminum channel, cut into two pieces, and locally manufactured carriers, which could be locked to the channel at any location along its length, were used to mount the optical equipment on the bench. One piece of channel, with mounts, supported the laser, beam expander, and mask on the open (mixing layer) side of the test section. The reducing telescope and camera were similarly mounted on the opposite side of the test section. This arrangement placed all optical elements in a straight line, eliminating the need for beam steering mirrors and minimizing the distance required between elements. Beam positioning and aiming were accomplished by

measuring the beam's entrance and exit locations on the test section and adjusting the input rail as required. The optical axis of the output rail was then adjusted to coincide with the axis of the input rail already established.

Filters: A BG-18 filter was placed at the camera to reduce infrared effects on the recorded image. In addition various neutral density filters were placed at the output lens of the reducing telescope to control the intensity of the laser beam before it arrived at the photodiode array.

Bias Illumination: It was found to be necessary to slightly bias the photodiode array with an additional "white" light source. This was done by placing a 12 volt DC incandescent light source in the field of view of the photodiode array. The illumination from this source passed through none of the optics other than the BG-18 infrared filter. This bias light source was powered by a voltage regulated DC power supply. The distance from the array to this light varied but was always greater than 1.5 meters. The exact distance was determined for each run by the combination of neutral density filters, array to reducing telescope distance, and bias light location that produced a well sized Airy pattern with a detectable first bright ring

and a peak intensity near but not exceeding the saturation level of the Microtex digitizer (see Data Acquisition Equipment). A "detectable" first bright ring was one which was apparent in the analog output of the camera as seen on an oscilloscope used for this purpose.

Data Acquisition Equipment:

Numerical data was obtained for later analysis through the use of a Microtex 7405 image acquisition system consisting of an analog to digital (A/D) conversion board and a logic board installed in a Digital Equipment Corporation MicroVAX I. The logic board provided all necessary signal and power output to operate the camera as directed by Microtex provided FORTRAN programs running in the MicroVAX computer. The digitized images output by the A/D converter were stored as data files in the MicroVMS operating system on the computer's hard disk. These data files contained integer values between 0 and 4096, representing the light intensity measured by each pixel in the 256x256 array.

IV. CALIBRATION AND CHECK OF EXPERIMENTAL SYSTEM:

Four separate checks were used to verify that the optics used were diffraction limited and that the image collected by the CCD array was indeed the Airy pattern of the diffraction mask.

First, since the largest diffraction mask aperture used was 1 cm in diameter, additional diffraction would not be induced by the 4.9 cm diameter large lens of the reducing telescope. And, with the objective lens being used the telescope has a power of 40, thus the waist of the reduced beam may be estimated as 0.25 mm, located at the small objective lens when the telescope is focused. Since this small lens has a diameter of 2.5 mm, it is 10 times the diameter of the beam waist and it adds no diffraction to the beam either.

Second, the distance, D , from the output of the reducing telescope to the far field was estimated using¹⁹:

$$D > \frac{4 a^2}{\lambda} \quad (7)$$

where:

λ = wavelength.

a = radius of the beam waist.

D = distance from the reducing telescope to the film.

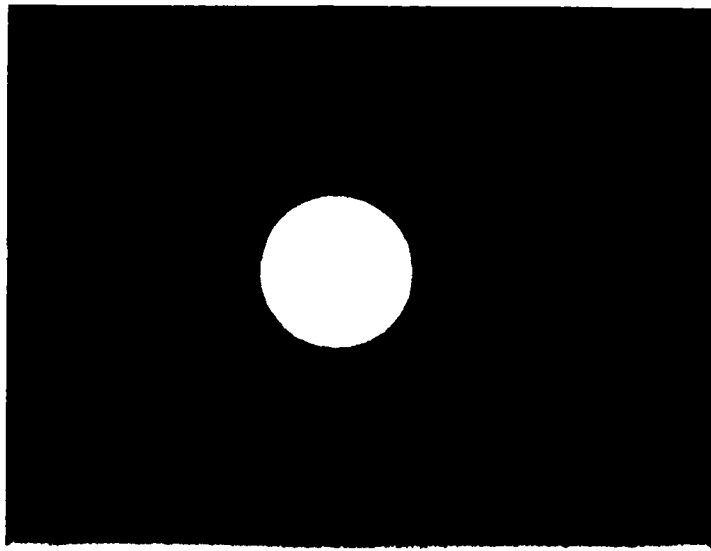
Since the distance from the telescope output was always greater than 30 cm for 0.5 cm diameter apertures and 50 cm for 1 cm apertures, the camera was safely in the far field if the reducing telescope was properly focused.

Third, a photographic image of the focused output of the telescope was analyzed to determine that the locations of the relative minima and maxima correspond to their theoretical locations for Airy patterns. Figure 5 is such a photograph. The aperture diameter was 0.5 cm and the distance of the film from the output lens of the 40 power reducing telescope was 201 cm. The measured radius to the center of the first dark ring, r_1 , is approximately 1.25 cm. A radius of 1.24 cm is predicted by the equation¹⁶:

$$r_1 = 1.22 \frac{D \lambda}{2 a} \quad (8)$$

Fourth, numerical integration of the intensity distribution in recorded images, as a function of radius,

Fig. 5. Airy pattern for a 0.5 cm diameter aperture at a distance of 201 cm from the output of a 40 power reducing telescope.



was compared to the theoretical prediction¹⁸ of the integration of the intensity pattern of Airy patterns. Figures 6 and 7a represent the "best" and "worst" of the results of such comparisons, respectively. In figures 6 and 7 the radius is represented by the nondimensional radius $x = kaw$, where k is the wave number, a is the radius of the beam waist, and w is the ratio of the actual radius and the distance from the reducing telescope.

Because the numerical integration of the camera pixel response was, by necessity, normalized to the total of the responses of pixels which fell within the largest circle that would fit on the array, plots like the one in figure 7a were very common. Notice however, that figure 6 encompasses three dark rings as indicated by the three flat spots in the theoretical curves. This indicates that the image in figure 6 has received 93.8% of the total energy in the original beam¹⁸. Figure 7a, on the other hand, encompasses only two dark rings indicating it has received 91% of the original beam energy. Figure 7b shows the comparison of theory to the numerical integration of the data when the numerical integration is normalized to the sum of the pixel responses divided by 0.91, the result is much nearer the theoretical curve. This further supports the assertion that the optics were diffraction limited.

Fig. 6. Intensity integration. Plot of the numerical integration of the pixel intensity response to an undistorted Airy pattern and theory. The theoretical curve rises faster at first, but reaches a lower maximum than the numerical integration of the data.

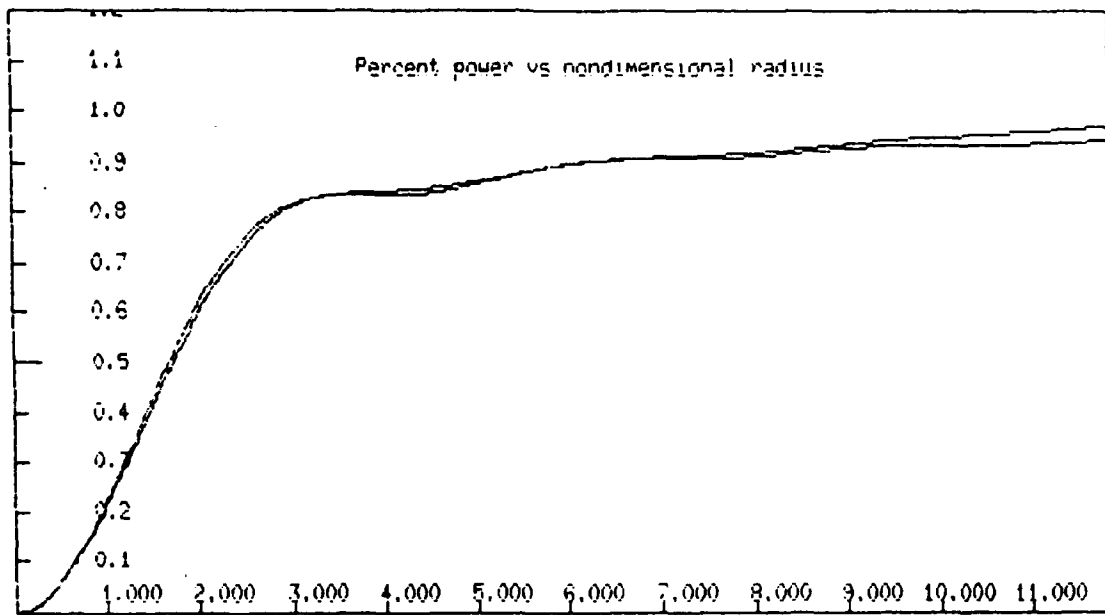
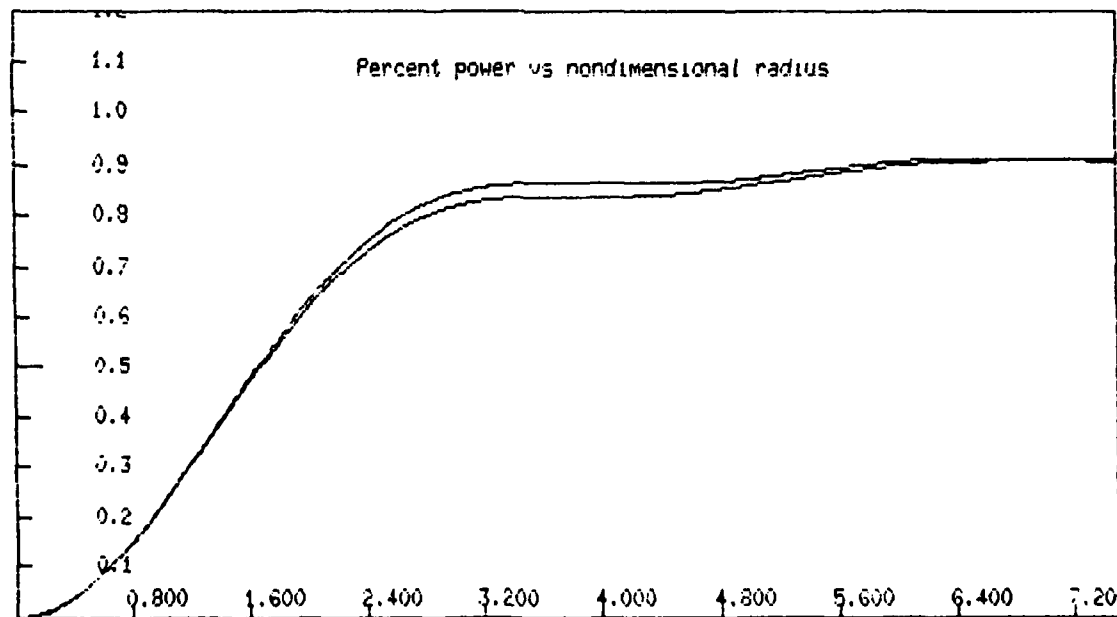
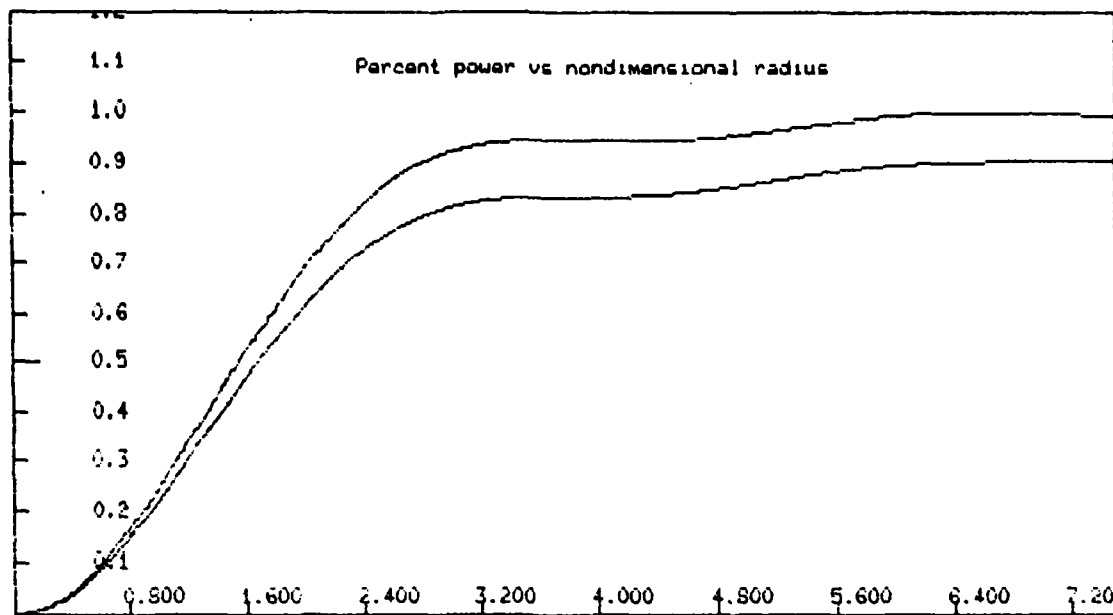


Fig. 7. Normalizing effect on intensity integration. Plot of the numerical integration of the pixel intensity response to an undistorted Airy pattern and theory. The data in 7a and 7b have been normalized by different values.

7a: The numerical integration of actual data rises to a higher value than the theory and approaches a value of 1.0, because it is normalized to the total light actually detected by the diode array. The theoretical curve however, is normalized to the total light contained in the beam.

7b: When the numerical integration of the actual data is multiplied by the theoretical ratio of the light contained within the second dark ring to the total light in the beam, the result much more closely resembles the theoretical curve.



Early experiments with the camera however, showed that while the array response was fairly linear as a whole, the level of dark current and random noise was not small in relation to the low signal strengths of the subsidiary maxima of the Airy patterns. Worse, the output of the array was not "flat" across its spatial dimensions. That is, the output of array elements or pixels near the horizontal center of the array had lower dark output levels than did pixels near either side of the array, and there was a definite high-low variation between even and odd numbered lines of pixels from top to bottom of the array. Finally, even though most of the output response of each of the pixels was fairly linear, at low input light levels this was not so and was not the same for each pixel. Because of these problems, a diffuse "white" light source was added to the optical table. It consisted of a pair of 6 volt incandescent bulbs powered in series by a voltage regulated, 12 volt DC power supply. This additional light had the two beneficial effects of: raising the reference output level of all pixels with no laser beam input to a nearly equal level across the array, and when added to the diffraction pattern of the laser beam, raising the first subsidiary maximum of the Airy pattern above the level of the dark current and random noise. The intensity of the additional light source seen by the camera was controlled

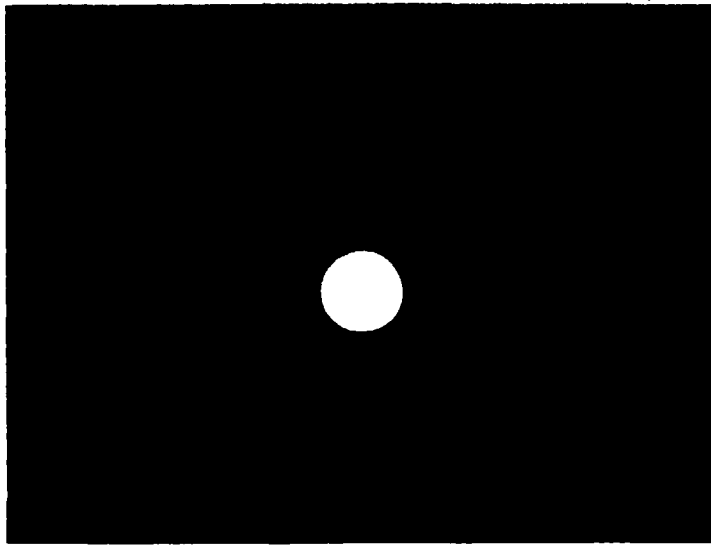
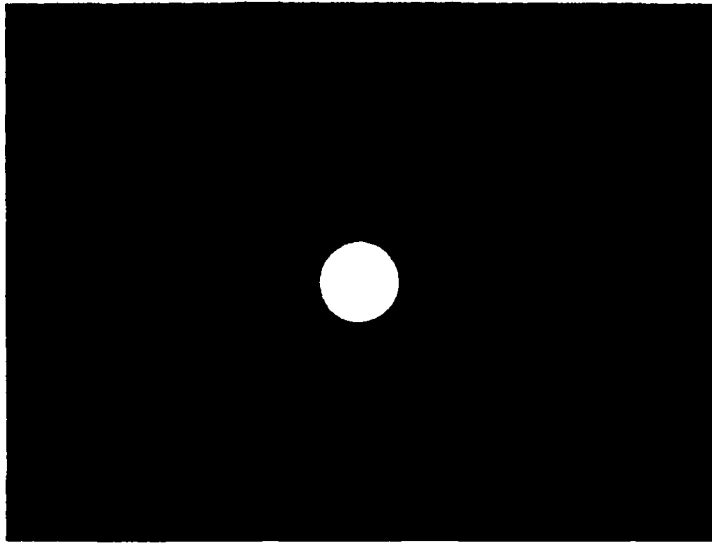
by varying the distance from the source to the camera so that the output of the camera with the laser turned off was nearly flat and with the laser turned on did not saturate the analog to digital converter board. The distance from the bulbs to the camera was not measured for each run but was on the order of two meters, and the maximum linear dimension of the two bulbs together was approximately 5 cm. This bias illumination was later subtracted numerically from the data. The plots in figures 6 and 7 were drawn after the bias was subtracted.

Acoustic noise generated by the operation of the nozzle was also a concern. Previous interferometry had been rendered useless by noise induced vibration in pieces of optical equipment. None of the equipment that had suffered from this in the past was used in this experiment, but to verify that the image distortion was not vibration induced, two photographs were taken with the beam passing just outside the glass walls of the test section. One photograph was taken with the jet turned off, the other with a helium jet running at a Mach number of nearly one, the most severe noise condition for this nozzle. These two photographs are shown in figure 8a and b.

Fig. 8. The effect of jet generated noise. Airy patterns of a beam passing nearby, but not through the test section

8a: Jet off (no noise)

8b: Helium jet on. Mach number nearly 1.



V. PROCEDURES:

The optical bench was aligned as follows:

A set of cross hairs was scribed on an aluminum target mounted on a slide mount that moved only parallel to the rail axis. After the laser was centered as closely as possible on the rail, aiming was done by rotating the laser until the unexpanded beam spot (approx 1 mm dia.) location on the target cross hairs moved less than one beam radius when the target was moved from one end of the rail to the other.

The beam expander was then added to the beam path. The beam expander was approximately aligned using back reflection from a reflective cap fitted over the input lens. Then, the input lens cap was removed and a cap with a 1 mm diameter hole in its center was placed over the output lens. The expander was then rotated while the target was slid back and forth again until the spot moved less than one spot radius. During this process, the beam expander was translated vertically or horizontally, as required, to maintain maximum intensity output as estimated by eye. The beam expander assembly contained a 25 micron spatial filter which was adjusted as required to maximize and center its output on the output lens, as estimated by eye.

With this done, all elements on the rail were locked in position and the horizontal location of the entrance of the 1 mm diameter beam into the test section was measured using a transparent plastic rule. Then one end of the rail was moved while the other was held fixed so that this location was centered on one side of the test section. That end of the rail was then fixed and the other end moved until the location of the beam exit was centered on the opposite side of the test section. By repeating this technique iteratively, the beam path through the test section was centered.

The rail on the output side of the test section was then fastened to the table approximately parallel to the first rail by the use of a straight edge. Final alignment of the second rail was done using the sliding target, and moving alternate ends of the rail, as before. The range of movement for the sliding target was approximately 40 cm on either rail.

The laser had previously been positioned so that the beam was normal to the jet and approximately 1 cm downstream of the nozzle exit. Now, the beam expander output lens cap was removed and a circular diffraction mask with a 1 mm diameter was inserted in the beam path and its vertical position adjusted so that the beam was measured to be 1 cm downstream of the nozzle exit.

Next, the reducing telescope was added to the beam path on the opposite side of the test section from the laser and was aligned using a lens cap having a 1 mm diameter hole in its center covered by a beam splitter. The reducing telescope was rotated and translated until the transmitted portion of the 1 mm beam passed through the 1 mm hole in the center of the lenscap and the reflected portion returned to the 1 mm hole in the diffraction mask.

Finally, the diffraction mask mount was so fabricated that masks with different diameters and center locations could be exchanged without disturbing the alignment of the rest of the beam. With the proper size and center location mask installed, the reducing telescope was focused and the CCD camera was positioned so that an appropriately sized image was centered on the array.

In order to reduce the effects of dark current, the camera was actively cooled by attaching a heat sink to the camera case and forcing cooled, dry nitrogen through fins in the heat sink. The nitrogen gas was cooled by passing through a tube immersed in liquid nitrogen. By this means, the camera case temperature was kept between 13 and 15 degrees Celsius. Without cooling, the camera case operating temperature was 40 to 50 degrees Celsius.

With the optics aligned and camera case temperature stabilized, a tare image (no gas flow in the nozzle), a

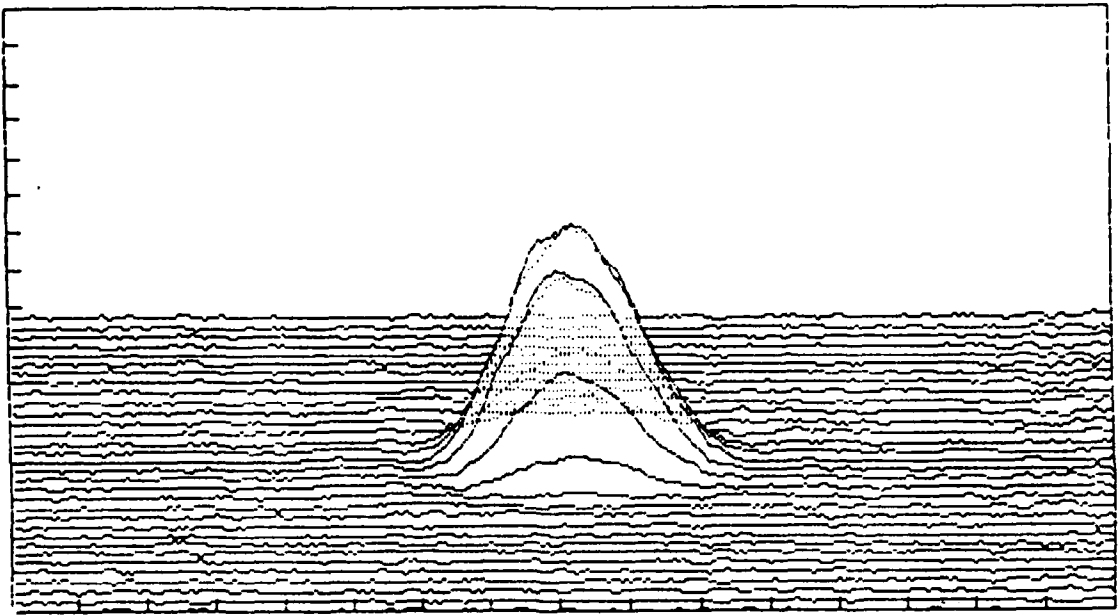
"flat field" reference image, and run images were taken and stored. For a run image, the gas supply to the nozzle was turned on and allowed to run for approximately one second. After this start-up period, the camera control software was initiated causing the camera to cycle through two images at the rate of 30 images per second, then the gas supply was turned off. Only the last image of the two was retained to minimize dark current errors. This image was digitized and stored as a 256 by 256 array on hard disk by the Microtex FORTRAN image management software. Except for gas flow in the nozzle, tare images and "flat field" reference images were taken and stored similarly. A tare image consisted of an undistorted Airy pattern and the bias illumination from the incandescent light source, a "flat field" reference image consisted of only the bias illumination from the incandescent light source. The "flat field" reference image was later subtracted numerically from both the tare and run images. A set of tare, reference, and run images was taken and stored for each run condition.

VI. DATA

Table 1 below, outlines the jet gas mixture, beam diameter, and location for which images were recorded. The extra images of a 1 cm diameter beam through a He jet at 1 cm downstream were taken to determine that the removal of one or more attenuator filters did not seriously effect either the beam deflection or Strehl ratio measurements. Since it did not seem to greatly effect the results, this technique was used (primarily for He jets) when the beam degradation was severe. The degradation caused by SF₆ jets however, was so severe that only a limited number of images using this gas were recorded, as table 1 indicates. All images were taken with a 1/30 second "exposure" time.

The recorded images may be visualised using pseudo-three-dimensional plots of the array response. Pixel response for every eighth line, for example, was plotted with the reference datum for each line shifted vertically by an amount proportional to the sine of some arbitrary view elevation angle. Figure 9 is an example of such a plot for a typical tare image (no flow) after the reference "flat field" has been subtracted. Ideally, figure 9 should be the pseudo-3-D plot of an Airy pattern¹⁸, but the subsidiary rings are not readily visible. However, evidence of ring structure did become

Fig. 9. Pixel response plot of every eighth row of a tare image. The aperture diameter was 1 cm, and the distance from the reducing telescope output lens was 51.5 cm. The reference image of the bias illumination has been subtracted from the actual data recorded by the camera.



apparent when the intensity distribution of the images were integrated with respect to radius, as is shown by the flat spots in the curves in figures 6 and 7 and all subsequent integrations of intensity for these images. Flat spots represent the near zero contribution to the integration from minima. A subsequent rise followed by another flat spot indicates a maximum. The integration technique is discussed further in the section on data reduction but, since the integration is radial, the maxima and minima are inferred to be ring shaped.

BEAM LOCATION	BEAM DIAMETER	
	1 cm	0.5 cm
x = 1	He(6), 62%He/38%Ar(3) 38%He/62%Ar(3), CO ₂ (3), SF ₆ (2)	He(3), 62%He/38%Ar(3), 38%He/62%Ar(3), CO ₂ (3), SF ₆ (3)
x = 2	He(3), 62%He/38%Ar(3) 38%He/62%Ar(3), CO ₂ (3)	He(3), 62%He/38%Ar(3), 38%He/62%Ar(3), CO ₂ (3)

Table 1. Test conditions. Numbers in parentheses indicate the number of images recorded for that combination of gas and beam parameters. Beam location, x, is in cm downstream from the nozzle exit.

Figures 10 and 11 were taken with the same mask aperture, downstream location, at the same distance from the telescope and under similar illumination, but with the jet on and the beam passing through the mixing layer. Thus, figures 10 and 11 may be compared to figure 9 for an appreciation of the beam degradation caused by mixing layers for 62% He/38%Ar and CO₂ jets at a location 1 cm downstream of the nozzle. However, each of the images represented by figures 10 and 11 had its own tare taken just previously for analysis purposes.

Of interest however, is the fact that the shape of the plot indicates that something more than simple dispersion of the beam is taking place, the cross section is no longer circular. As the distortion caused by the mixing layer becomes more severe, it also becomes more complex. Some of the images of degraded beams contained what appeared to be two peaks, but at much lower intensities than the undistorted beam.

Figure 12a and b are photographs under similar illumination and with the same aperture size and downstream location as the images plotted in figures 10 and 11. Figure 12a was taken with no flow and figure 12b with the beam passing through a CO₂ jet. These photographs are provided as further subjective evidence of the fidelity of the recorded digital images. The two smaller spots in the

Fig. 10. Pseudo-3-D intensity plot for 62%He/38%Ar
jet, 1 cm diameter beam, 1 cm downstream of nozzle
exit.

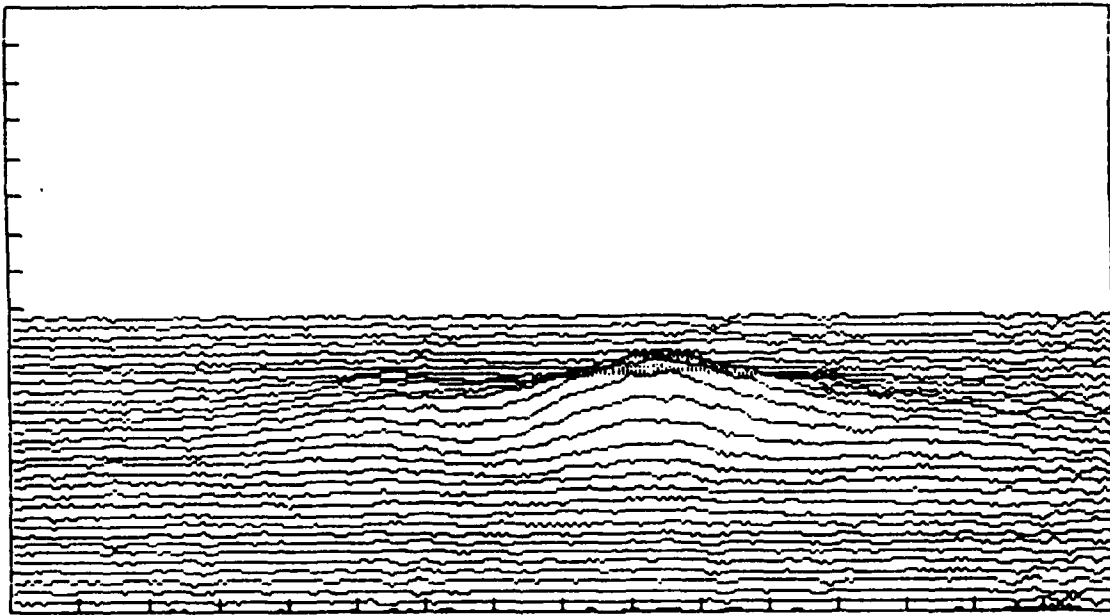


Fig. 11. Pseudo-3-D intensity plot for CO₂ jet, 1 cm diameter beam, 1 cm downstream from nozzle exit.

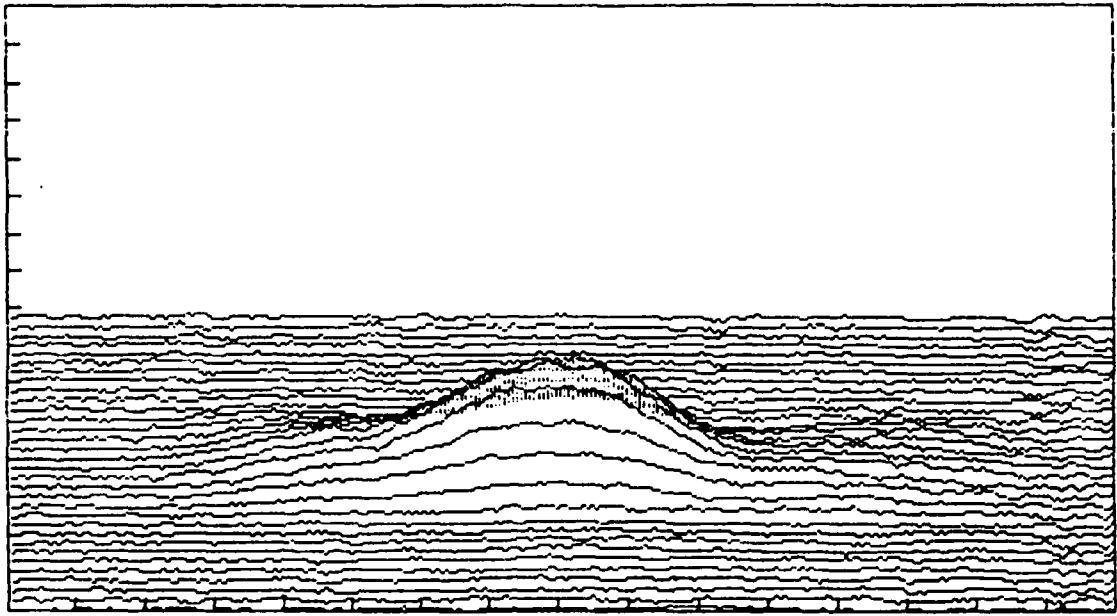
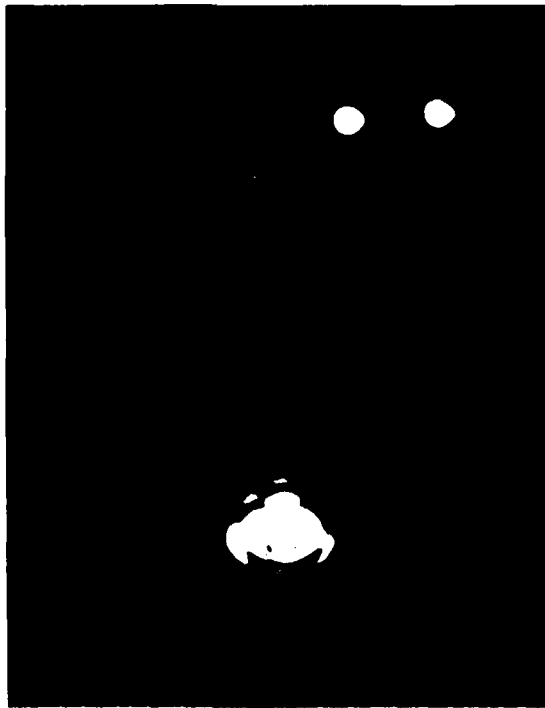
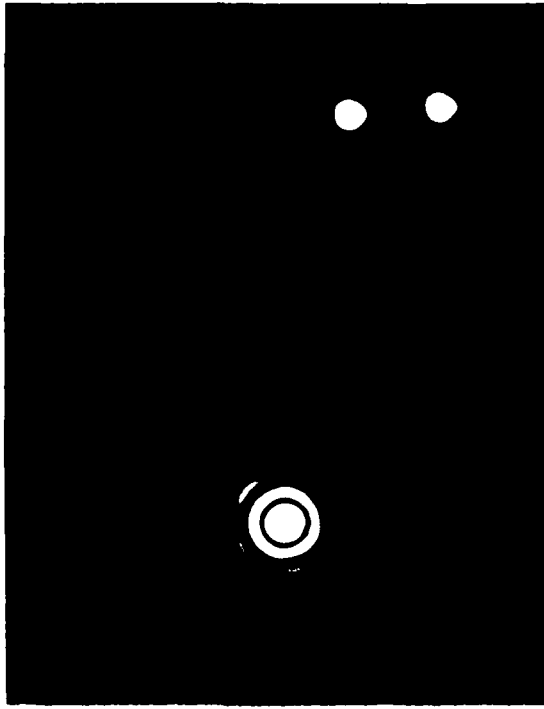


Fig. 12. Beam distortion resulting from a CO₂ jet.
The center peak has been deliberately overexposed to
show subsidiary ring structure.

12a: Undistorted tare.

12b: 1 cm diameter beam, 1 cm downstream from nozzle
exit.



upper portion of the photographs in figure 12 are reference spots used to gauge the displacement of the distorted beam maximum. They are approximately 1.1 cm apart on the original photographs and are not themselves displaced from the tare to the jet-on condition.

Figures 13 through 17 are plots of images taken with the same size mask aperture, but at 2 cm downstream from the nozzle. The pixel response in figure 13 has been enhanced by the removal of a 5x attenuator filter after taking its tare, but before taking the image for which figure 13 is the plot.

Photographs, similar to figure 12, were taken of the farfield for each of the experimental conditions. While these photographs offer little in the way of quantitative intensity distribution data, they correspond in overall structure to the digital images that were recorded. Therefore, the pseudo-3-D plots and the digitized images they represent are believed to be reasonable representations of the far field intensity distributions of the degraded beams.

Fig. 13. Pseudo-3-D intensity plot for He jet, 1 cm diameter beam, 2 cm downstream from nozzle exit. The response has been effectively amplified in comparison to other images at similar conditions by the removal of a 5x attenuator filter prior to exposure.

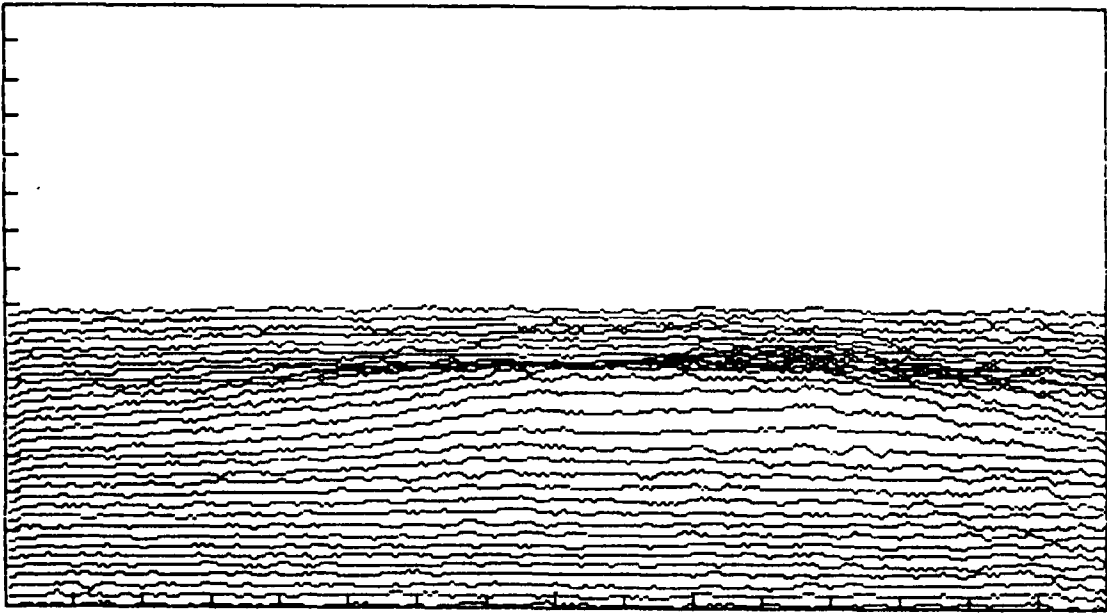


Fig. 14. Pseudo-3-D intensity plot for 62%He/38%Ar jet, 1 cm diameter beam, 2 cm downstream from nozzle exit.

Fig. 15. Pseudo-3-D intensity plot for 38%He/62%Ar jet, 1 cm diameter beam, 2 cm downstream from nozzle exit.

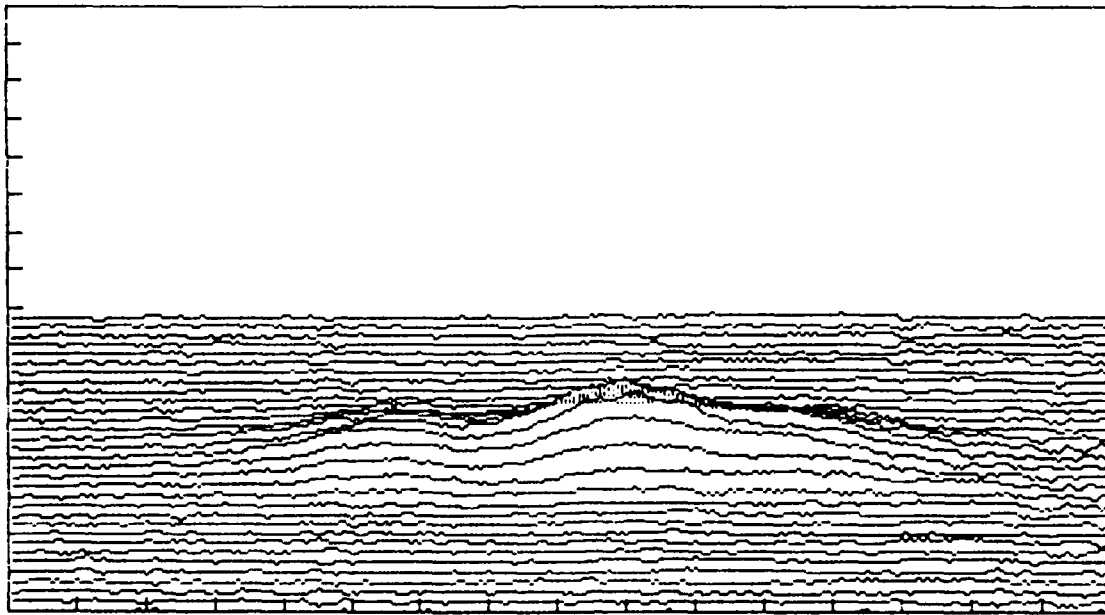
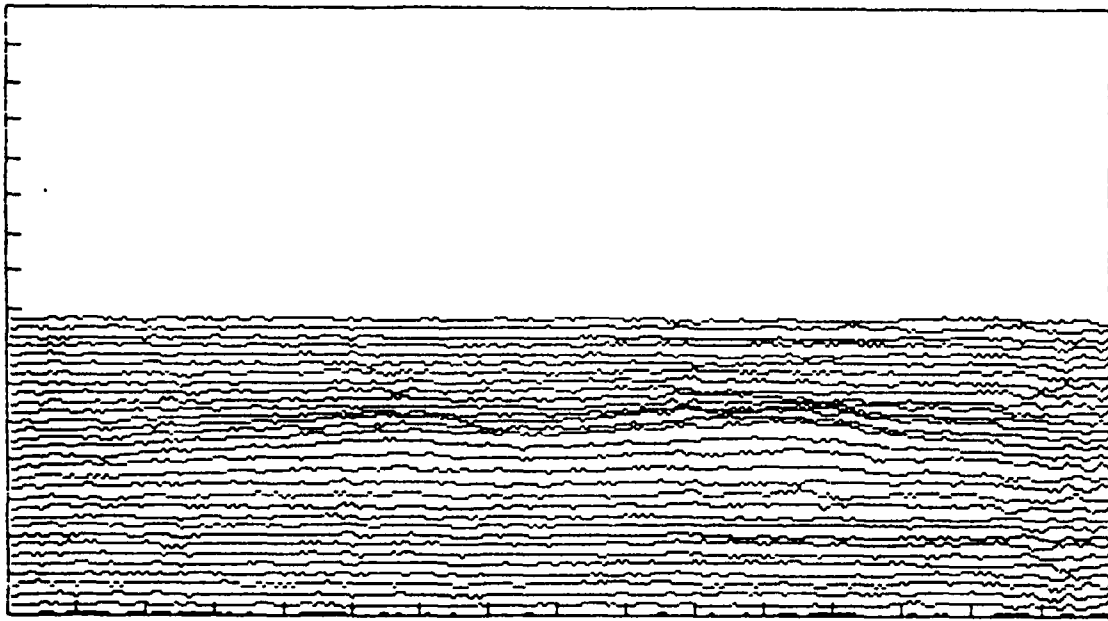
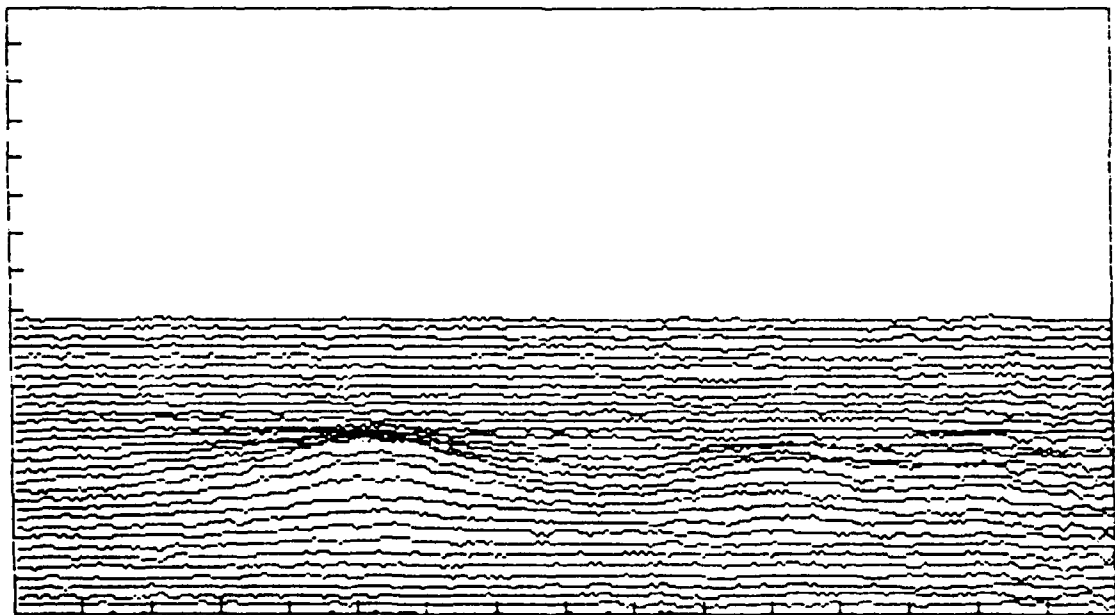
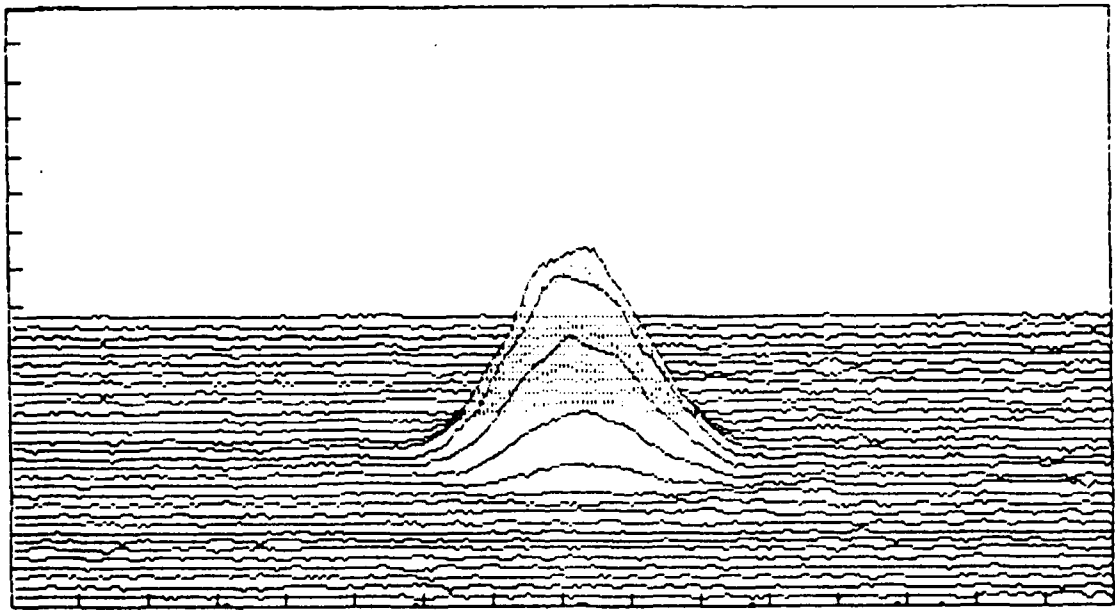


Fig. 16. Pseudo-3-D intensity plot for N₂ jet, 1 cm diameter beam, 2 cm downstream from nozzle exit.

Fig. 17. Pseudo-3-D intensity plot for CO₂ jet, 1 cm diameter beam, 2 cm downstream from nozzle exit.



VII. DATA REDUCTION

One of the ways to represent beam degradation is the Strehl ratio⁴. The Strehl ratio is the ratio of the intensity of the distorted beam intensity at the center of the far field focus to the undistorted beam intensity at the center of the far field focus. This ratio is significant because it is a measure of the effect of the RMS phase front error across the aperture on the "center line" intensity of the beam. A Strehl ratio of 1.0 indicates no effect, or no phase front error; as the RMS phase front error increases, the Strehl ratio will decrease.

The simple approach to obtaining the Strehl ratio from the recorded data would be to note the location of the tare image peak intensity and then divide the distorted beam intensity recorded at this location by the tare peak intensity. However, this would ignore any deflection or tilting of the beam as a result of passing through the mixing layer. Ideally, then, the easiest way to obtain the Strehl ratio would be to take the ratio of the peak distorted beam intensity and the peak tare intensity regardless of where they occurred. This was not practical here. Not only was it not practical because of the lack of "flatness" of array's response across its spatial

dimensions and because of the odd-even response of alternate lines, but because it was found that some aspect of the image capture and digitization system caused a drift in the zero datum level of successive frames that could not be quantified on a pixel by pixel basis. In order to correct for this, the following approach was used:

1. The location of the intensity centroid of the pixels having recorded intensity values not less than 90% of the maximum value recorded for the image was determined numerically.

2. The curves like those plotted in figures 6 and 7 were developed by a summation process of the form,

$$P(m\Delta r) = \sum_s \sum_t I_{st} : \sqrt{(k-s)^2 + (l-t)^2} < m\Delta r \quad (9)$$

where:

I_{st} = the recorded intensity at the pixel located in the s 'th row and the t 'th column.

I_{kl} = the intensity of the pixel located nearest the centroid of the peak of the intensity distribution.

k = the row number of the location of the centroid of
the peak of the intensity distribution.

l = the column number of the location of the centroid
of the peak of the intensity distribution.

$n = 1, 2, 3, \dots, 1000.$

$\Delta r = \min(i_{\max}, j_{\max})/1000.$

i_{\max} = least number of rows between k and either edge
of the array.

j_{\max} = least number of columns between l and either
the top or bottom of the array.

This summation approximated the integral relationship,

$$P(r) = \int_0^r I(\xi) 2 \pi \xi d\xi \quad (10)$$

Since

$$\frac{dP}{dr} = 2 \pi r I \quad (11)$$

then,

$$\lim_{r \rightarrow 0} \left[\frac{\frac{dP}{dr}}{\frac{dP_t}{dr}} \right] = \frac{I}{I_0} \quad (12)$$

where:

P = is the value of P for the degraded beam,

P_t = the value of P for the tare,

3. The limit in eqn. (11) was then estimated graphically by plotting the ratio

$$\frac{P(n\Delta x)}{P_t(n\Delta x)} \quad (13)$$

versus the nondimensional radius, x , given by:

$$x = kaw$$

where:

k = the wave number,

a = the diameter of the beam waist,

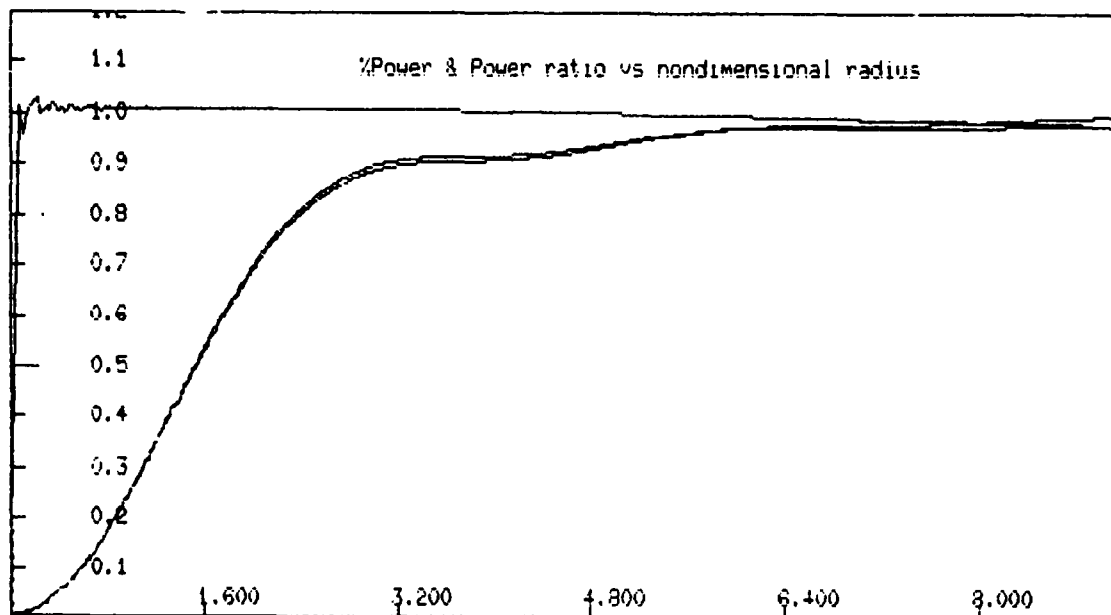
$w = r/D$, the ratio between the radius and the distance from the beam waist.

It was important to estimate the Strehl ratio graphically because of the extreme variations in the ratio in the limit, eqn. (11), as r approached Δr . These variations are due to the non-continuous nature of the digitized data as a function of the non-continuous parameter $n r$. As an example of how this was done, two separate images of the same undegraded beam were recorded and the integrated intensities and ratio of integrated intensities are plotted in figure 18.

Figure 18 shows three curves. The two curves which are initially lowest are plots of the normalized, numerical integration of the beam intensities over the radius as functions of radius. The upper, nearly horizontal, curve is the ratio of the the integrated intensities as a function of radius.

In this figure, the Strehl ratio of two images taken from the same undegraded beam, but at different times, is estimated from the plot of the ratio of the integrated intensities, or powers, of each beam as a function of radius. This curve is the numerical approximation of the ratio in expression (12). The theoretical value of the Strehl ratio in this case is, of course, 1.0, and the graph

Fig. 18. Power plots for an undegraded beam.
Normalized power and power ratio (or %power) plots for
two images of the same undegraded beam.

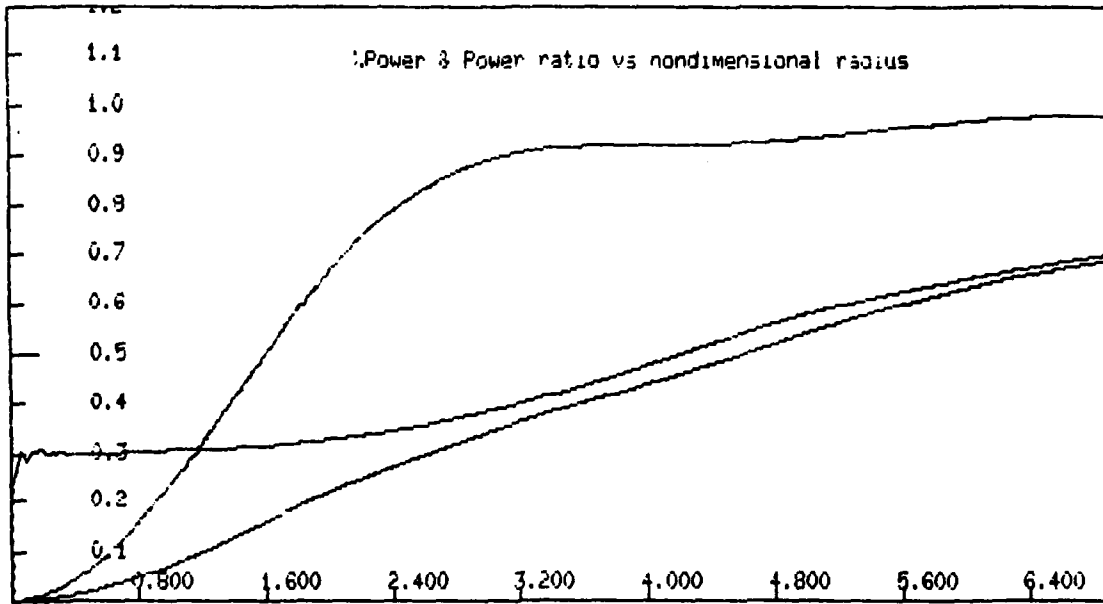


can be seen to approach that value in spite of the "noise" near the limit as r approaches 0.

Another example of this graphical technique for estimating Strehl ratio, using actual degraded beam data, is shown in figure 19. For reference, this is the plot used to estimate the Strehl ratio for the image whose pseudo-3-D intensity plot is shown in figure 10. A similar plot was generated for each digitized image that was recorded. The Strehl ratios for the recorded images were obtained by estimating the value that the plot of the power ratio tended toward as the value of the radius became small.

Tables 2 and 3 present a summary of the results of the analysis of all of the recorded data. For each combination of experimental conditions, the average of the estimated Strehl ratios is tabulated.

Fig. 19. Normalized power and power ratio plots for an undegraded target and a 1 cm beam 1 cm downstream in a 62%He/38% He jet. This is the radial integration of figure 10.



DOWNSTREAM DISTANCE = 1 cm

GAS	DENSITY RATIO	APERTURE DIAMETER	
		0.5 cm	1 cm
		AVG STREHL RATIO	AVG STREHL RATIO
He	7.22	0.35	0.13
62%He/38%Ar	1.64	0.60	0.31
38%He/62%Ar	1.10	0.84	0.74
N ₂	1.03	0.99	0.99
CO ₂	0.65	0.79	0.48
SF ₆	0.2	0.18	0.05

Table 2. Average values of Strehl ratios measured at 1 cm downstream from nozzle exit.

DOWNSTREAM DISTANCE = 2 cm

GAS	DENSITY RATIO	APERTURE DIAMETER	
		0.5 cm	1 cm
		AVG STREHL RATIO	AVG STREHL RATIO
He	7.22	0.22	0.07
62%He/38%Ar	1.64	0.40	0.15
38%He/62%Ar	1.10	0.66	0.34
N ₂	1.03	1.0	0.97
CO ₂	0.65	0.44	0.20

Table 3. Average values of Strehl ratios measured at 2 cm downstream from nozzle exit.

VIII. DISCUSSION

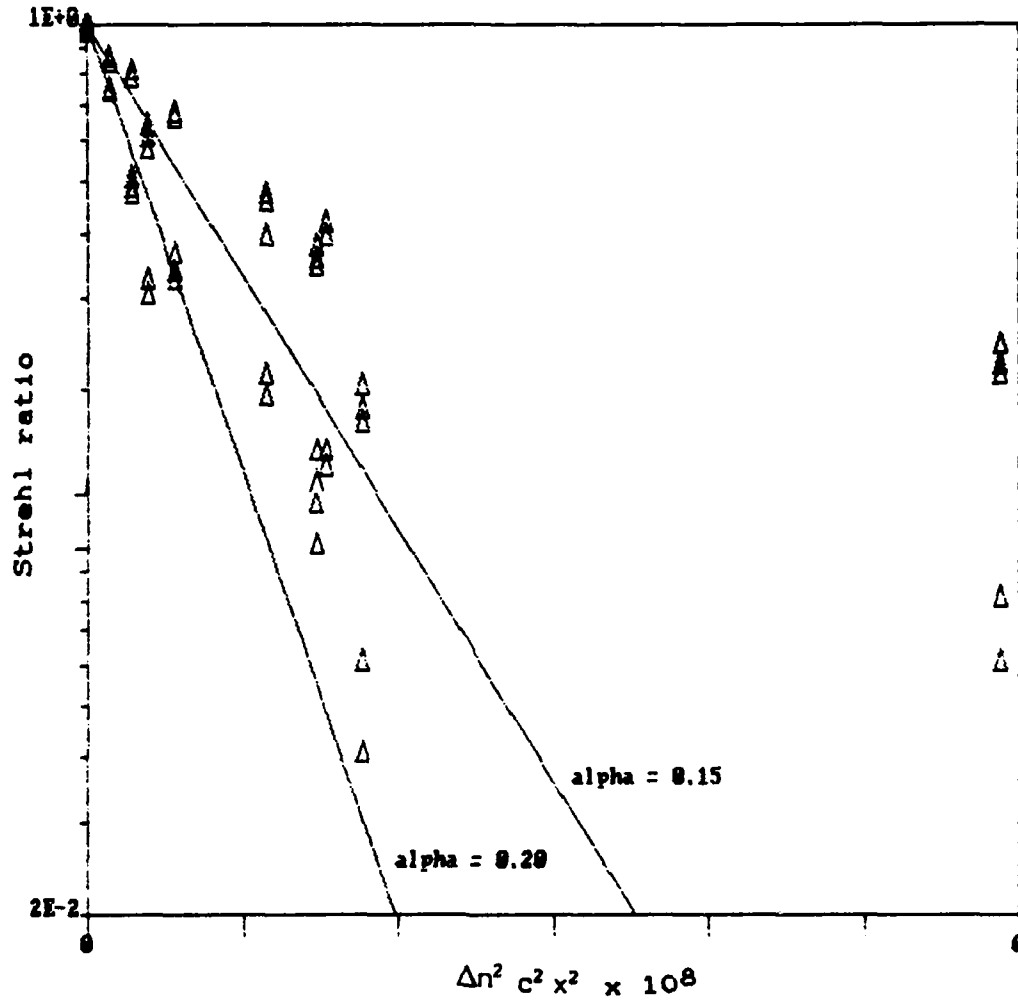
The estimated Strehl ratio values from the data are plotted versus $\Delta n^2 c^2 x^2$ in figure 20 along with curves for eqn. (6) using values for $\alpha = 0.15$ and $\alpha = 0.20$. The value for c used for eqn. (6) in these plots, as a function of density ratio was determined from the three data points on the spreading rate given by Brown and Roshko¹⁰ and the following curve fit function:

$$c = 0.38 + 0.14 \log \frac{p_2}{p_1} + \log^2 \frac{p_2}{p_1} \quad (14)$$

Note that eqns. (5) and (6) predict that aperture size should have no effect on the Strehl ratio since aperture size does not appear in the equation. However, examination of figure 20 reveals that for each value of $\Delta n^2 c^2 x^2$, the measured data tends to fall into two groups: a higher value of Strehl ratio, and a lower value. The higher grouping always corresponds to the smaller aperture size, and the lower grouping to the larger aperture.

Fig. 20. Measured Strehl ratios and graphs of equation (6) for two values of alpha.

MEASURED STREHL RATIOS vs Equation (6)



It should also be noted that the approach used to estimate the Strehl ratio assumes that the peak intensity centroid is the center of the far field focus, as does the measurement of beam deflection mentioned below. This may not be the case, but should be a close approximation to the tilt correction required by the definition of the Strehl ratio. Furthermore, in the cases where the beam was no longer even circular its not clear how one would define the center of the far field focus.

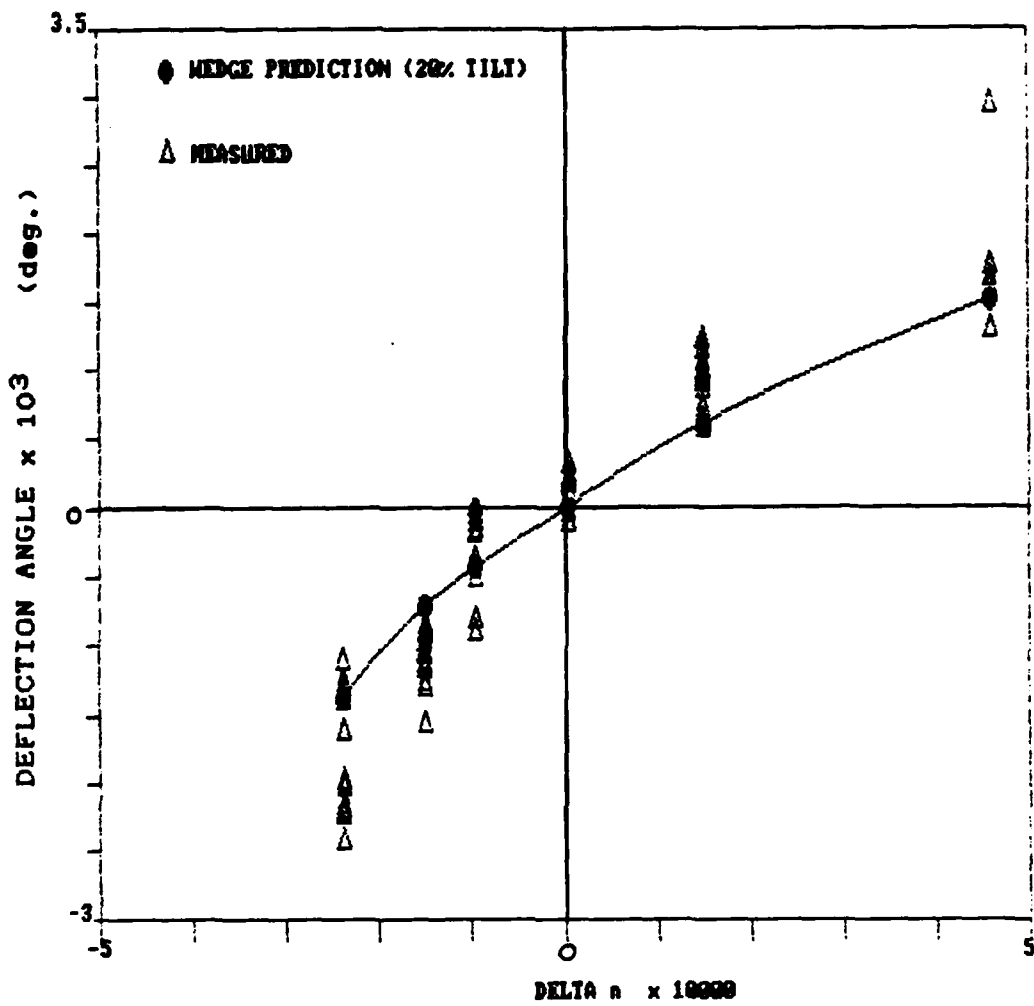
Measured beam deflection data for all of the test conditions are plotted in figure 21. Negative values of Δn (DELTA n on the plot) indicate jet gases with indices of refraction less than that of air, while positive values indicate that the jet had a larger index of refraction than air. The deflection angle is the angle the beam was tilted away from the nozzle, as determined by the movement of the location of peak intensity. Hence, negative deflection angles indicate that the beam was deflected toward the nozzle.

It is interesting to note that eqn. (4) predicts that a homogeneous wedge perpendicular to the beam will not deflect the beam. But, as the wedge is tilted, eqn. (4) predicts increasing beam deflection. Further, if the tilt of the wedge is away from the jet at an angle of approximately 20% of the total wedge angle the beam

deflections predicted by eqn. (4) are very close to the measured beam deflections. Such a tilt is consistent with the shapes of mixing layers seen by Poling² using the same nozzle as was used here.

Fig. 21. Measured beam deflections. Positive deflections are away from the nozzle.

BEAM DEFLECTION



IX. CONCLUSIONS

The Strehl ratios measured in this work, and plotted in figure 20, show roughly the same variation with $\Delta n^2 c^2 x^2$ as is predicted by Sutton in eqn. (6), except for the He jet data taken at 2 cm downstream. It is likely that a value of α could be found for each of the other test conditions which would make the match for the remaining data even closer, as it is possible that the turbulence intensity varied from jet to jet. However, α was not measured. And, it is generally held³ that the presence of coherent structure, as was the case here, reduces the validity of eqn. (6) as a predictor of beam degradation. Further, the data demonstrate a variation with beam diameter not predicted by eqn. (5) or eqn. (6).

The He jet data considered to be the exception are the data at the far right in figure 20. The intensity distribution for the beam after passing through the He jet 2 cm downstream is nearly indistinguishable from the background, even after the removal of a 5x attenuator filter. This is shown by figure 13 which is the pseudo-3-D intensity plot for one of these images. These data are considered to be highly suspect because the recorded data is so close to the noise level of the array output.

The measured beam deflections also show a trend similar to a prediction model, that of a simple wedge with two optical interfaces. However the wedge in this simple model must be tilted away from the jet and toward the incoming beam in order to match the data. This seems to be a reasonable requirement based on the observed shape of actual mixing layers.

Here, an arbitrary tilt angle for the wedge, equal to 20% of the total wedge angle, was chosen because it seems natural that the amount of tilt would depend on the same parameters that determine the wedge angle, and the factor of 20% fit the data. A more complex model using a finite number of small wedges may do a better job of modeling the beam deflection. This would be a problem of quadrature though, because the beam angle of incidence for each of the wedges would depend on the angle of transmission from the preceding wedge.

In all, the results of this work validate the concept of photo sensor arrays as sensors to directly sample the far field distortion caused by turbulent interfaces. And, it provides direct experimental data verifying in general the dependencies identified by Sutton¹⁷ and Vu et. al⁶. However, it suggests the possibility of other dependencies associated with the size of the beam relative to some length dimension of the mixing layer. The nature of this

dependency was not discovered.

Further work on the development of this technique and its use to expand the range of experimental conditions, primarily various density ratios at higher Mach numbers, is warranted.

REFERENCE LIST

1. Parmentier, E.M. and Greenberg, R.A., "Supersonic Flow Aerodynamic Windows For High Power Lasers," AIAA Journal, vol II, 1973, pp 943-949.
2. Poling, H.W., "Optical Properties of Shear Layers," Masters Thesis, University of Washington, 1985.
3. Christiansen, W.H., Johari, H., and Bogdanoff, D.W., "A Study of Inhomogeneous Shear Layers and Their Effects on Laser Beam Degradation," Inst. Phys. Conf. Ser. No. 72, 5th GCL Symp., Oxford, 1984.
4. Goodman, J.W., Introduction to Fourier Optics, McGraw-Hill, San Francisco, 1968
5. Legner, H.H., Otis, J.H., Theophanis, G.A., and Feinberg, R.M., "Laser Beam Degradation Through Turbulent Interfaces," AIAA Paper 78-71, 1978.
6. Vu, B.T., Sutton, G.W., Theophanis, G., and Limpacher, R., "Laser Beam Degradation Through Optically Turbulent Mixing Layers," AIAA Paper 80.1414, 1980.

7. Wasserstrom, E. and Christiansen, W.H., "Phase Correction of a Laser Beam by Gas Jets," AIAA Paper 81-4011, 1981.
8. Geargeoura, J.E., "Laser Beam Degradation in Supersonic Free Jets," Master's Thesis, University of Washington, 1980.
9. Tritton, D.J., Physical Fluid Dynamics, Van Nostrand Reinhold (UK), Berkshire, 1982.
10. Brown, G.L. and Roshko, A., "On density effects and large structure in turbulent mixing layers," Journal of Fluid Mechanics, vol. 64, 1974, pp. 775-816
11. Breidenthal, R., AA 508: Lectures on Turbulent Flow, University of Washington, 1985.
12. Bradshaw, P., "The effects of initial conditions on the development of a free shear layer," Journal of Fluid Mechanics, vol 26, 1966.
13. Schlichting, H, Boundary Layer Theory, McGraw-Hill, Inc., New York, 1979.

14. Liepmann, H.W. and Roshko, A., Elements of Gas Dynamics, Wiley, New York, 1952.
15. Batt, R.G., "Turbulent mixing of passive and chemically reacting species in a low-speed shear layer," Journal of Fluid Mechanics, vol. 82, 1977, pp. 53-95.
16. Fiedler, H.E., "Transport of Heat Across a Plane Turbulent Shear Layer," Advances in Geophysics, vol. 18a, 1974, pp. 93-109.
17. Sutton, G.W., "Effect of Turbulent Fluctuations in an Optically Active Medium," AIAA Journal, vol. 7, 1969, pp 1737-1743.
18. Born, M. and Wolf, E., Principles of Optics, Pergamon Press, Oxford, 1970.
19. Hecht, E., Theory and Problems of Optics, McGraw-Hill, New York, 1975.

END

DITIC

9 - 86